

A FURTHER DROP INTO QUIESCENCE BY THE ECLIPSING NEUTRON STAR 4U 2129+47

JINRONG LIN¹, MICHAEL A. NOWAK¹, DEEPTO CHAKRABARTY¹*Accepted by ApJ 2009, October*

ABSTRACT

The low mass X-ray binary 4U 2129+47 was discovered during a previous X-ray outburst phase and was classified as an accretion disk corona source. A 1% delay between two mid-eclipse epochs measured ~ 22 days apart was reported from two *XMM-Newton* observations taken in 2005, providing support to the previous suggestion that 4U 2129+47 might be in a hierarchical triple system. In this work we present timing and spectral analysis of three recent *XMM-Newton* observations of 4U 2129+47, carried out between November 2007 and January 2008. We found that absent the two 2005 *XMM-Newton* observations, all other observations are consistent with a linear ephemeris with a constant period of 18 857.63 s; however, we confirm the time delay reported for the two 2005 *XMM-Newton* observations. Compared to a *Chandra* observation taken in 2000, these new observations also confirm the disappearance of the sinusoidal modulation of the lightcurve as reported from two 2005 *XMM-Newton* observations. We further show that, compared to the *Chandra* observation, all of the *XMM-Newton* observations have 40% lower 0.5–2 keV absorbed fluxes, and the most recent *XMM-Newton* observations have a combined 2–6 keV flux that is nearly 80% lower. Taken as a whole, the timing results support the hypothesis that the system is in a hierarchical triple system (with a third body period of at least 175 days). The spectral results raise the question of whether the drop in soft X-ray flux is solely attributable to the loss of the hard X-ray tail (which might be related to the loss of sinusoidal orbital modulation), or is indicative of further cooling of the quiescent neutron star after cessation of residual, low-level accretion.

Subject headings: accretion, accretion disks – stars:individual(4U 2129+47) – stars:neutron – X-rays:stars

1. INTRODUCTION

4U 2129+47 was discovered to be one of the Accretion Disk Corona (ADC) sources (Forman et al. 1978), which are believed to be near edge-on accreting systems since they have shown binary orbital modulation via broad, partial V-shape X-ray eclipses (Thorstensen et al. 1979; McClintock et al. 1982, hereafter MC82, White & Holt 1982); the eclipse width was ≈ 0.2 in phase and $\approx 75\%$ of the X-rays were occulted at the eclipse midpoint. The origins of ADCs are not fully understood, but they are typically associated with high accretion-rate systems, wherein we are only observing the small fraction of the system luminosity that is scattered into our line of sight. For the prototypical ADC X1822–371, models suggest that it is accreting at a near Eddington rate, with the radiation scattered into our line of sight having an equivalent isotropic luminosity on the order of 1% of the total luminosity (see Parmar et al. 2000; Heinz & Nowak 2001; Cottam et al. 2001, and references therein).

In the early 1980s, observations of 4U 2129+47 showed that both its X-ray and optical lightcurves were modulated over a 5.24 h period (Thorstensen et al. 1979; Ulmer et al. 1980; McClintock et al. 1982; White & Holt 1982). The discovery of a type-I X-ray burst led to the classification of 4U 2129+47 as a neutron star (NS) low mass X-ray binary (LMXB) system (Garcia & Grindlay 1987), and the companion was suggested to be a late K or M spectral type star of $\sim 0.6M_{\odot}$. The source distance was estimated to be ~ 1 –2 kpc (Horne et al. 1986). Assuming isotropic emission, the X-ray luminosity would have then corresponded to $\sim 5 \times 10^{34}$ ergs⁻¹. Even if the luminosity were 100 times larger, the luminosity would have been somewhat smaller than expected for an ADC.

Since 1983, 4U 2129+47 has been in a quiescent state. Optical observations show a flat lightcurve without any evidence for orbital modulation between the years 1983 and 1987. Additionally, instead of an expected M- or K-type companion, the observed spectrum was compatible with a late type F8 IV star (Kaluzny 1988; Chevalier et al. 1989). The refined X-ray source position as determined by *Chandra* turned out to be coincident with the F star to within 0.1" (Nowak, Heinz, & Begelman 2002, hereafter N02). The probability of a chance superposition is less than 10^{-3} (see also Bothwell et al. 2008), therefore, the hypothesis of a foreground star is unlikely. A ~ 40 km s⁻¹ shift in the mean radial velocity was derived from the F star spectrum, providing evidence for a dynamical interaction between the F star and 4U 2129+47 (Cowley & Schmidtke 1990; Bothwell et al. 2008). The system was therefore suggested to be a hierarchical triple system, in which the F star is in a month-long orbit around the binary (Garcia et al. 1989). This hypothesis is tentatively confirmed with two *XMM-Newton* observations separated by 22 days that showed deviations from a simple orbital ephemeris (Bozzo et al. 2007, hereafter B07). Assuming that the F star is part of the system, the source distance was revised to ~ 6.3 kpc (Cowley & Schmidtke 1990). This would imply that the peak luminosity observed prior to 1983 (assuming that the observed flux was $\sim 1\%$ of the average flux) was a substantial fraction of the Eddington luminosity. The X-ray spectrum of 4U 2129+47, as determined with a *Chandra* observation taken in 2000, was consistent with thermal emission plus a powerlaw hard tail (N02). The 2–8 keV flux was $\approx 40\%$ of the 0.5–2 keV absorbed flux. The contribution of the “powerlaw” hard tail to the 0.5–2 keV band was, of course, model dependent, but was consistent with being $\approx 20\%$ of the 0.5–2 keV flux, as we discuss below. A sinusoidal orbital modulation (peak-to-peak amplitude of $\pm 30\%$) was observed in the X-ray lightcurve in the same observation.

¹ Massachusetts Institute of Technology, Kavli Institute for Astrophysics and Space Research, Cambridge, MA 02139, USA; jinrongl@mit.edu; mnowak.deepto@space.mit.edu

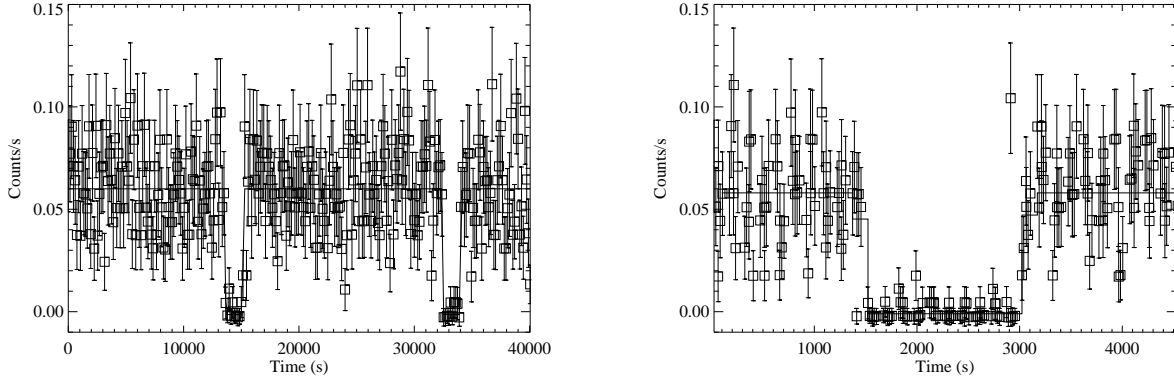


FIG. 1. — a) Left: Lightcurve from one of the 2007 *XMM-Newton* observations, fit by a total eclipse with finite duration ingress and egress. No sinusoidal orbital modulation was evident. The 90% confidence level upper limit of the modulation is 10%. b) Right: Lightcurve of six eclipses folded as one. The mid-eclipse epochs are aligned and centered at 2250 s.

The phase resolved spectra showed variation in the hydrogen column density. However, in the *XMM-Newton* observations (B07), the sinusoidal modulation was absent, while the flux of the powerlaw component was constrained to be less than 10% of the 0.2–10 keV flux (B07).

Here we report on recent *XMM-Newton* observations of 4U 2129+47. We combine analyses of these observations with reanalyses of the previous observations, and show that, absent the two 2005 *XMM-Newton* observations (B07), the historical observations are consistent with a linear ephemeris with a constant period. We outline our data reduction procedure in §2 and present the timing and spectral analysis in §3 and §4 respectively. We summarize our conclusions in §5.

2. OBSERVATIONS AND DATA

XMM Newton observed 4U 2129+47 on Nov 29, Dec 20, 2007 and on Jan 04, Jan 18, 2008. The total time span for each of these 4 observations was 43270 sec, resulting in effective exposure times of at least 30 ksec for the EPIC-PN, EPIC-MOS1, and EPIC-MOS2 cameras for the first three observations. The remaining observing time was discarded due to the background flares. The standard *XMM Newton* Science Analysis System (SAS 8.0) was used to process the observation data files (ODFs) and to produce calibrated event lists. We used the EMPROC task for the two EPIC-MOS cameras and used the EPPROC task for the EPIC-PN camera. We used the high energy ($E > 10$ keV) lightcurves to determine the Good Time Intervals, so as to obtain the event lists that were not affected by background flares. The Good Time Intervals are slightly different for EPIC-PN and EPIC-MOS cameras; therefore, the overlap Good Time Interval was used to filter each lightcurve with the EVSELECT keywords “timemin” and “timemax”.

The low energy (0.2–1.5 keV) source lightcurves and the spectra (0.2–12 keV) were extracted within the circles of $14.6''$ radius centered on the source. Larger circles were not used in order to avoid a Digital Sky Survey stellar object (labeled as S3- β in N02). We extracted background lightcurves and spectra within the same CCD as the source region. The largest source-free regions near the source, which were within circles of radii about $116''$, were chosen for background extraction. The SAS BACKSCALE task was performed to calculate the difference in extraction areas between source and background. In order to obtain the mid-eclipse epochs, we tried various bin sizes (75 s, 150 s and 300 s etc.) to obtain the best compromise between signal to noise ratio in a bin, and

time resolution. Finally the lightcurves were extracted with the bin size of 150 s. The times of all lightcurves were corrected to the barycenter of the Solar System by using the SAS BARYCEN task. Lightcurves from EPIC-PN and two EPIC-MOS cameras were summed up with the LCMATH task, in order to get better statistics in the fitting of the eclipse parameters. Given the low count rate of the EPIC-MOS cameras compared to the EPIC-PN camera, for the spectral analysis we discuss only the spectrum from the EPIC-PN camera.

3. ORBITAL EPHEMERIS AND ECLIPSE PARAMETERS

The observation made on Jan 18, 2008 was seriously affected by background flares, however, 2 eclipses were found in each of the other 3 observations respectively, resulting in 6 eclipses for fitting.

The 3 pairs of eclipses were then simultaneously fit with the same set of eclipse parameters. The ingress duration, the egress duration, and the duration of the eclipse (defined to be from the beginning of the ingress to the end of the egress) were set to be free parameters and assumed to be the same for all 6 eclipses, under the hypothesis that these eclipses should have the same shape (see §5). The starting time of the first eclipse ingress and the count rates within and out of the eclipse were fit for each lightcurve individually. The separation between the two connected eclipses within the same lightcurve was set to be 18857.63 s based upon the previous *Chandra* results. The second eclipse in each lightcurve therefore only contributed to the fitting of the eclipse shapes, while only the first eclipse in each lightcurve has been used to estimate the orbital ephemeris. The mid-eclipse epoch was defined to be the starting time of the ingress plus half of the eclipse full ingress-to-egress duration. The model was integrated over each time bin, especially the bins that are crossed by the ingress and the egress, in order to be compatible with either the finite ingress/egress durations or the infinite ingress/egress slopes (for a rectangular eclipse model). χ^2 minimization was performed in order to determine the best fit to the lightcurve.

One of our fitted lightcurves is shown in Fig. 1a. The best fits to the mid-eclipse epochs were found to be $T_0(1) = 2454\,433.8640 \pm 0.0004$ JD, $T_0(2) = 2454\,455.6900 \pm 0.0004$ JD and $T_0(3) = 2454\,470.0948 \pm 0.0004$ JD, with $\chi^2/\text{d.o.f.} = 782.6/708$ (errors are at 68% confidence level). The best fit result favors a rectangular eclipse model with very short duration of the ingress and egress durations; upper limits of 50 s and 30 s were found for the ingress and egress

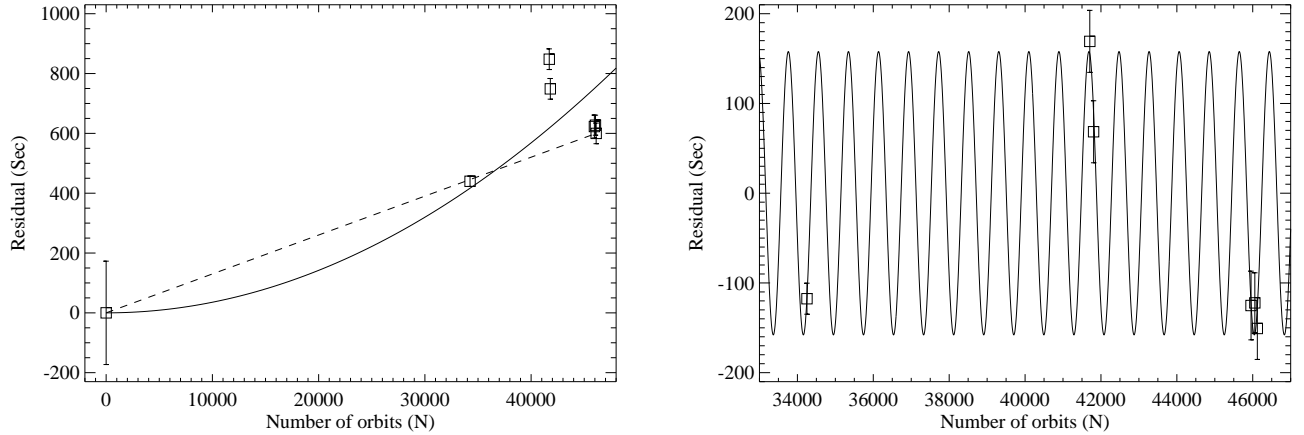


FIG. 2.— Each square shows the timing residual (defined as the difference between the observed ephemeris and the predicted ephemeris) at certain number of orbits from the observations listed in Table 1. a) Left: The dashed line denotes a linear ephemeris with a period of 18857.63, while the solid line denotes a quadratic ephemeris. Absent the 2005 *XMM-Newton* observations, the ephemeris of the eclipses can be well fitted by a constant period. However, we confirmed the strong deviations of the 2005 *XMM-Newton* observations from any linear or quadratic ephemeris. b) Right: Close up of the third body fit with a third body period of ~ 175 days, showing just the *Chandra* and *XMM-Newton* data since year 2000. The solid line denotes a sinusoidal ephemeris.

TABLE 1
MID-ECLIPSE EPOCH MEASUREMENTS.

Observatory	Mid-eclipse Epoch (JD)	Orbital Period (sec)	References
<i>Einstein</i>	2444403.743(2)	18857.48(7)	(MC82)
<i>Chandra</i>	2451879.5713(2)	18857.631(5)	(N02)
<i>XMM-Newton</i>	2453506.4821(4) ^a	18857.638(7)	(B07) ^a
<i>XMM-Newton</i>	2453528.3069(4) ^a	18857.636(7)	(B07) ^a
<i>XMM-Newton</i>	2454433.8640(4)	18857.632(7)	this work
<i>XMM-Newton</i>	2454455.6900(4)	18857.632(7)	this work
<i>XMM-Newton</i>	2454470.0948(4)	18857.631(7)	this work

NOTE. — Numbers in parentheses are the errors (at 1σ level) on the last significant digit.

^a We reprocessed the data for these two observations using a 150 s binned lightcurves in order to be consistent with our routine.

durations respectively. A folded lightcurve of 6 eclipses is shown in Fig. 1b, where the mid-eclipse epochs are aligned and centered. The sinusoidal variation seen in the *Chandra* observation is absent; the upper limit of the modulation amplitude is $< 10\%$ at 90% confidence level. The duration of the eclipses were derived to be 1565 ± 23 s. We also re-analyzed the previous two *XMM-Newton* observations of May 15 and June 6, 2005 with the above methods in order to get a direct comparison with our data sets. These two lightcurves were also extracted with 150 s bins, and there was one eclipse present in each of them. The best fit mid-eclipse epochs are $T_0(a) = 2453\,506.4821 \pm 0.0004$ JD and $T_0(b) = 2453\,528.3069 \pm 0.0004$ with $\chi^2/\text{d.o.f.} = 18.8/21$ and $87.8/84$, respectively.

We considered the above mid-eclipse epochs together with epochs, T_n , derived from the previous observations (Table 1) in order to determine a refined orbital solution and to measure any orbital period derivative (which was weakly suggested by the analysis of N02). We considered the ephemeris from MC82 as reference ($T_{ref} = 2444\,403.743 \pm 0.002$ JD, $P_{ref} = 18\,857.48 \pm 0.07$ s), and calculated n , the closest integer to $(T_n - T_{ref})/P_{ref}$. Our three observations (the first eclipse in each of the three lightcurves) correspond to $n =$

45 955,46 055,46 121. The average orbital periods ($P = (T_n - T_{ref})/n$) inferred from these observations are therefore 18857.632 ± 0.005 s, 18857.631 ± 0.005 s and 18857.632 ± 0.004 s. We noticed that, absent the 2005 *XMM-Newton* observations, the 2007/2008 observations are consistent with a linear ephemeris with a constant period of 18 857.63 s. However, we confirmed the strong deviations of the 2005 *XMM-Newton* observations from any linear or quadratic ephemeris (Fig. 2). We therefore tried to fit the linear timing residual by a third body orbit on top of a steady binary orbital period. For simplicity, we assume the interaction between a binary system and a third body results in a sinusoidal residual. The ephemeris is not uniquely determined; we found valid ephemerides for the third body orbit at ~ 800 , 1300, 1700, 1900, and 2900 times the binary orbit. The shortest consistent sinusoidal period was therefore found to be ~ 175 days (Fig. 2).

4. SPECTRAL ANALYSIS

The spectra of the 3 observations were accumulated during the same time intervals selected for the extraction of the EPIC-PN lightcurves, except that the eclipses were also excluded. Spectral analysis was carried out using ISIS version 1.4.9-55 (Houck & Denicola 2000). Since there is no evidence of orbital modulation in the lightcurves, the spectra we produced were not phase resolved. Furthermore, preliminary fits indicated little or no variability among spectra from individual observations; therefore, we fit all spectra simultaneously. Specifically, we used the ISIS `combine_datasets` functionality² to sum the spectra and responses during analysis. The data were binned to have a minimum signal-to-noise³ of

² This is essentially equivalent to summing the pulse height analysis (PHA) files and summing the product of the response matrix and effective area files. Whereas this can be accomplished, e.g., using `FTOOLS` outside of the analysis program (and in fact, “outside of analysis” is the only mode supported by `XSPEC`), performing summing during analysis allows one to examine data and residuals for each data set individually, choose different binning and noticing criteria based upon individual spectra, etc.

³ To be explicit, here and throughout we mean that the source counts, excluding the estimated background counts, divided by the estimated error, including that of the background counts, meets or exceeds the given signal-to-noise threshold in each spectral bin.

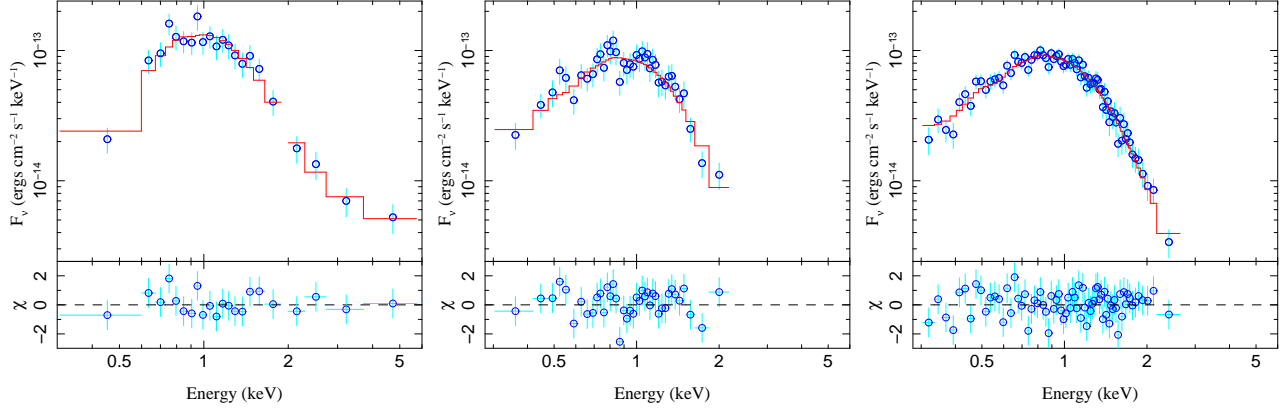


FIG. 3.— Combined spectra for the *Chandra* observations of Nowak, Heinz, & Begelman (2002) (left), the *XMM-Newton* observations of Bozzo et al. (2007) (middle), and the three *XMM-Newton* observations presented in this work (right). Each has been fit with a model consisting of an absorbed blackbody plus powerlaw; however, the photon index is fixed to $\Gamma = 2$ for the *XMM-Newton* observations. Note that all spectra have been unfolded without reference to the underlying fitted spectral model. (The unfolded spectra do, however, reference the response matrices of the detectors; see Nowak, et al. 2005 and the Appendix for further details.)

4.5 and a minimum of four energy channels per grouped spectral bin. The spectra were fit over an energy range such that the lower bounds of the spectral bins exceeded 0.3 keV, and the upper bounds of the spectral bins were less than 8 keV. (This latter criteria, with the above grouping, effectively restricted the upper bound of the spectra to be ≈ 3 keV.)

The spectra could be well-fitted by an absorbed blackbody, both with and without a powerlaw (Table 2). For the absorption, following the fits of N02, we used the model of Wilms, Allen, & McCray (2000). Given that the presence of any powerlaw was not well constrained, we froze its photon index to $\Gamma = 2$ when including such a component in the fits. Without the additional powerlaw, the best fit temperature and column density were $0.21^{+0.01}_{-0.01}$ keV and $(0.21 \pm 0.02) \times 10^{22} \text{ cm}^{-2}$, with a $\chi^2 = 62.6/73$ degrees of freedom. With the additional powerlaw, the best fit temperature and column density were $0.20^{+0.01}_{-0.01}$ keV and $(0.24 \pm 0.03) \times 10^{22} \text{ cm}^{-2}$, with a $\chi^2 = 57.8/73$ degrees of freedom. Both of these sets of parameters are consistent with the thermal component of the fits presented by N02 for the *peak* (i.e., least absorbed part) of the sinusoidal modulation of the *Chandra* lightcurve. We show the spectra and fit including the powerlaw in Fig. 3.

As indicated by these fits (all of which have reduced $\chi^2 < 1$), the powerlaw hard tail is no longer required to describe the spectrum. Including a powerlaw slightly increases the best fit N_{H} and its associated error bars, while slightly decreasing the best fit temperature. Our best fit models, with or without a powerlaw, yield an absorbed 0.5–2 keV flux of $(7.7 \pm 0.1) \times 10^{-14} \text{ ergs cm}^{-2} \text{ s}^{-1}$, with no more than 10%, i.e., $0.7 \times 10^{-14} \text{ ergs cm}^{-2} \text{ s}^{-1}$ (90% confidence level) being attributable to a $\Gamma = 2$ powerlaw. This 0.5–2 keV flux is 36% lower than the $(1.2 \pm 0.1) \times 10^{-13} \text{ ergs cm}^{-2} \text{ s}^{-1}$ found during the peaks of the *Chandra* lightcurve (see below). Note that above, and throughout this work, unless stated otherwise we will quote 68% confidence limits for fluxes, but 90% confidence limits for fit parameters.

To estimate the 2–6 keV flux, we grouped the spectrum (starting at 2 keV) to have a minimum signal-to-noise of 3 and a minimum of 2 channels per grouped energy bin, and then we fit an unabsorbed powerlaw spectrum between 2–6 keV. (Grouping to higher signal-to-noise left no channels between ≈ 3.5 –6 keV.) This yields an estimated $(6 \pm 3) \times 10^{-15} \text{ ergs cm}^{-2} \text{ s}^{-1}$ in the 2–6 keV band, which is to be com-

pared to the nearly five times larger 2–6 keV flux of $(2.9 \pm 0.6) \times 10^{-14} \text{ ergs cm}^{-2} \text{ s}^{-1}$ from the *Chandra* observations (see below).

The question then arises as to when the drop in the 0.5–2 keV flux occurred, and whether or not it is solely attributable to the loss of the hard X-ray tail. To further explore these issues, we applied absorbed blackbody plus powerlaw fits to the spectra described by B07 (out of eclipse data only, grouped and noticed exactly as for the 2007/2008 *XMM-Newton* spectra described above, with powerlaw index frozen to $\Gamma = 2$), and refit the spectra of N02 (powerlaw index left unfrozen). We used the same exact data extractions and spectral files from N02. For the *Chandra* observations, we follow N02 and fit the 0.3–2 keV spectra (grouped to signal-to-noise of 4.5 at 0.3 keV and above) from the peak of the lightcurve’s sinusoidal modulation, while we fit the 2–6 keV spectra (grouped to a signal-to-noise of 4 at 2 keV and above) from all of the out of eclipse times. The flux levels quoted above correspond to these new fits of the *Chandra* data.

The fits to the data from B07 are completely consistent with the fits to the new data, and yield a blackbody temperature and neutral column of $0.21^{+0.01}_{-0.03}$ keV and $0.27^{+0.09}_{-0.04} \times 10^{22} \text{ cm}^{-2}$, respectively, with $\chi^2 = 32.2/37$ degrees of freedom. The powerlaw normalization was consistent with 0, and thus excluded a powerlaw from the fits to these data. The absorbed 0.5–2 keV flux was $(7.5 \pm 0.3) \times 10^{-14} \text{ ergs cm}^{-2} \text{ s}^{-1}$, i.e., comparable to that from the more recent *XMM-Newton* data. The spectra are shown in Fig. 3.

As discussed in N02, and shown in Fig. 3, the *Chandra* data clearly indicate the presence of a hard tail. Here we find $N_{\text{H}} = 0.39^{+0.18}_{-0.11} \times 10^{22} \text{ cm}^{-2}$, $kT = 0.21^{+0.03}_{-0.04}$ keV, and $\Gamma = 2.0^{+1.5}_{-1.6}$, with $\chi^2 = 10.7/17$ degrees of freedom. Note that the larger N_{H} value found here compared to N02 is due to the inclusion of the 0.3–0.5 keV data, and is partly indicative of a systematic dependence of this parameter upon the index of the fitted powerlaw. For the best-fit powerlaw index, $0.2 \times 10^{-14} \text{ ergs cm}^{-2} \text{ s}^{-1}$ of the 0.5–2 keV absorbed flux is attributable to the powerlaw. This is not enough to account for the drop in flux between the *Chandra* and *XMM-Newton* observations. However, if for the *Chandra* spectra we fix the powerlaw at its 90% confidence level upper limit ($\Gamma = 3.5$), then $0.6 \times 10^{-14} \text{ ergs cm}^{-2} \text{ s}^{-1}$ of the 0.5–2 keV absorbed flux is attributable to the powerlaw component (albeit

with an $N_{\text{h}} = 0.58 \times 10^{22} \text{ cm}^{-2}$, which is higher than the best fit values for the *XMM-Newton* data). This is more than enough to account for all of the change in the 0.5–2 keV absorbed flux, and highlights some of the systematic uncertainties inherent in determining bolometric flux changes (i.e., the need to adequately model the changes in the local column and to use realistic models for the hard X-ray tail). With these current data, it is difficult to distinguish between resumed cooling of the neutron star thermal component, or mere loss of the additional (presumed external) hard tail component that here is modeled with a powerlaw.

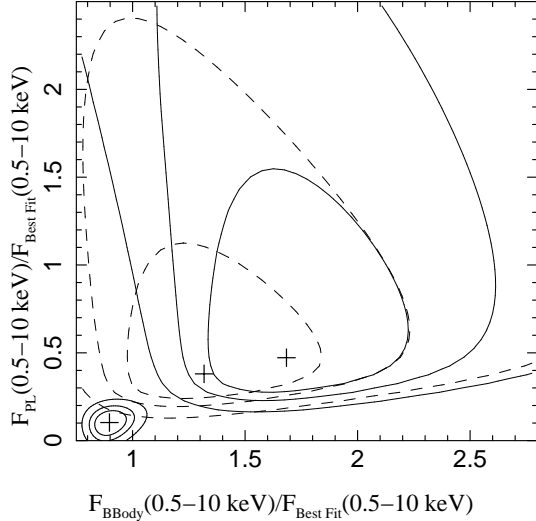


FIG. 4.— 68%, 90%, and 99% confidence contours for the *unabsorbed* 0.5–10 keV flux in the blackbody (x-axis) and powerlaw (y-axis) components from fits to the 0.3–6 keV spectra from the 2007/2008 *XMM-Newton* observations (lower left) and *Chandra* observation (upper right). The dashed confidence contours correspond to fits to the 0.6–6 keV band of the *Chandra* spectra. Plus signs indicate the “best fit” values. Note that all flux values are shown relative to the total, unabsorbed flux in the 0.5–10 keV band determined from the best blackbody plus powerlaw fit to the 2007/2008 *XMM-Newton* observations.

To highlight some of the issues with determining bolometric flux changes and with attributing any changes to specific model components, in Fig. 4 we show error contours for the *unabsorbed* 0.5–10 keV flux in the blackbody and powerlaw components when fitting the 2007/2008 *XMM-Newton* spectra and the *Chandra* spectra. These errors account for uncertainties in the neutral column, but do not address systematic issues with the choice of model itself. We see that formally the 99% confidence level contours *do not overlap*, which would indicate that *both* the thermal and powerlaw components have decreased between the time of the *Chandra* and *XMM-Newton* observations. However, if we ignore the first bin (0.3–0.6 keV) in the *Chandra* spectra, the *Chandra* contours shift significantly leftward towards lower blackbody flux. (Additionally, the fitted neutral column also decreases.) There is less of a shift downward in powerlaw flux between these two fits of the *Chandra* data. Thus, as stated above, it remains somewhat ambiguous as to what extent the changes between the *Chandra* and *XMM-Newton* data can be attributed solely to components other than the thermal emission from the neutron star.

We have fit also the *XMM-Newton* spectra with the neutron star atmosphere (NSA) model of Zavlin, Pavlov, & Shibano (1996), by fixing the neutron star distance to 6.3 kpc and the

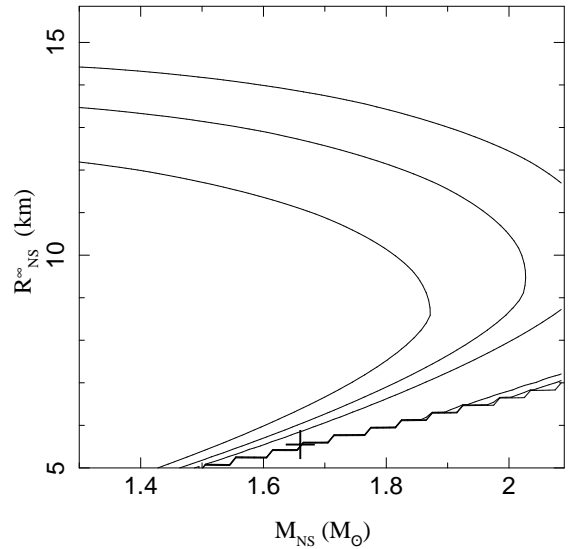


FIG. 5.— 68%, 90%, and 99% confidence contours for the neutron star mass (x-axis) and radius (y-axis) from neutron star atmosphere (NSATMOS) model fits to the 0.3–6 keV spectra from the 2007/2008 *XMM-Newton* observations. The neutron star distance was fixed to 6.3 kpc. The plus sign corresponds to the best fit. The jagged contours at the bottom of the figure represent the limits of the interpolation grids used in the calculations of the NSATMOS model.

neutron star mass to $1.4 M_{\odot}$. Results of these fits are presented in Table 2. They are consistent with those of N02 and B07 (although N02 also required the inclusion of a powerlaw component). Specifically, we find neutron star radii of ≈ 5 km, and effective temperatures in the range of $2\text{--}3 \times 10^6$ K. If we instead use the NSATMOS model of Heinke et al. (2006), again fixing the neutron star mass and distance as above, we find lower neutron star temperatures ($\approx 10^6$ K) and significantly larger radii (> 12 km). This raises the question of the degree to which one can find a consistent fitted mass and radius among all the datasets discussed here.

To explore this question, we have performed a joint fit of the *Chandra* and *XMM-Newton* spectra. The observations from the individual observing epochs (2000, 2005, 2007/2008) were grouped and added as described above, with the additional caveat that we now exclude the *Chandra* data below 0.6 keV so as to minimize the influence of the soft-end of the powerlaw component on the fitted neutral column. We include a hard tail, modeled as a $\Gamma = 2$ powerlaw, in fits to the *Chandra* spectra, and again use the NSATMOS model (Heinke et al. 2006) to describe the soft spectra from all epochs. For this latter component we again fix the distance to 6.3 kpc and we further constrain the neutron star mass and radius to be the same for all epochs. The individual epochs, however, are fitted with independent neutron star temperatures and neutral columns. Results are presented in Table 3.

We find that one can find a set of consistent parameters that are statistically acceptable. There is a modest need for the *Chandra* spectra to be described with a slightly larger neutral column than that fit to the 2007/2008 *XMM-Newton* spectra. The *Chandra* spectra also require a slightly higher neutron star temperature, but here all temperatures fall within each others error bars. The best fit mass is $1.66 M_{\odot}$ and the best fit radius is 5.55 km. This is somewhat smaller than the values presented in Table 2 when applying the NSATMOS model with a fixed mass of $1.4 M_{\odot}$, and is more consistent with the values found when using the NSA model.

The reasons for this can be elucidated by examining the er-

ror contours for the fitted mass and radius. In Fig. 5 we show the mass/radius contours obtained from applying an absorbed NSATMOS model to just the 2007/2008 *XMM-Newton* data (i.e., our best measured spectrum, with no discernible hard tail). We see that the error contours admit a wide range of masses and radii, with the curvature of these contours generally favoring two regimes: small radius (with high temperature - not shown in this figure) and large radius (with lower temperature). Formally, the small radius/high temperature solution is the statistical minimum; however, it is not statistically very different than the large radius/low temperature regime. (Comparable contours for the NSA model look very similar, albeit with the contours shifted to lower mass values.)

These different fit parameter regimes add further systematic uncertainty to estimates of the unabsorbed, 0.5-10 keV flux. As shown in Tables 2 and 3, the estimate of this flux ranges from $1.5\text{--}1.9 \times 10^{-13} \text{ erg cm}^{-2} \text{ s}^{-1}$ for the 2007/2008 *XMM-Newton* data alone. Furthermore, we see that depending upon whether we use a phenomenological model (the blackbody plus powerlaw fits) individually fit to each epoch, or a more physical model (e.g., NSATMOS) jointly fit to all epochs, we either find evidence for further neutron star cooling or evidence of a consistent neutron star surface temperature. We again caution, however, that determining the bolometric flux in specific model components can be fraught with many systematic uncertainties (e.g., Fig. 4), and we therefore consider any evidence for further neutron star cooling to be ambiguous at best.

5. CONCLUSIONS

We reported on recent *XMM-Newton* observations of 4U 2129+47 in a quiescent state. Given lower background flaring rates and relatively longer durations of these observations compared to the 2005 *XMM-Newton* observations reported by Bozzo et al. (2007), we were able to make clear the following three points:

1. The 0.5–2 keV absorbed X-ray flux of the source has been reduced by more than $\approx 40\%$ compared to the *Chandra* observation. This was even true for the observations discussed by B07.
2. The sinusoidal variation seen in the *Chandra* observation ($\pm 30\%$ peak-to-peak) is absent, or at least greatly diminished (90% confidence level upper limits of $\pm 10\%$ modulation). Additionally, the associated neutral column exhibits no orbital variability, and is consistent with the brightest/least absorbed orbital phases of the *Chandra* observation.
3. The powerlaw tail seen in the *Chandra* observation is absent. A $\Gamma = 2$ powerlaw contributes less than 10% of the 0.5–2 keV flux, and is not evident in the 2–6 keV band. The 2–6 keV flux is reduced by a factor of five compared to the *Chandra* observation.

With this further drop in the X-ray flux of the source, we may now truly be seeing 4U 2129+47 enter into a quiescent stage solely dominated by neutron star cooling, with little or no contribution from residual weak accretion. The spectrum of the source can be well explained by absorbed blackbody emission from the surface of a neutron star, with an emission radius of ~ 1.8 km. Likewise, more sophisticated neutron star

atmosphere models also describe the spectra very well, with no need for an additional component.

As discussed by N02, the sinusoidal variability detected with the *Chandra* observation could have been due to a neutral hydrogen column being raised by the interaction of the accretion stream with the outer edge of an accretion disk (Parmar et al. 2000; Heinz & Nowak 2001). The fact that the sinusoidal modulation was absent in the 2007, and likely also the 2005 *XMM-Newton* observations could suggest that the system is in a lower accretion state, and might indicate that the geometry of the outer disk region has changed. It has been hypothesized that the hard tails of quiescent neutron stars originate from a pulsar wind, only able to turn on in quiescence, that is interacting with the accretion stream at large radius (Campana et al. 1998; Campana & Stella 2000). The vanishing of both the hard tail and the sinusoidal modulation in 4U 2129+47 could suggest that what we had observed in the *Chandra* observation was indeed the interaction between the pulsar wind and the disk edge, perhaps as the last remnants of a disk accreted onto the neutron star. This is consistent with the fact that for these current *XMM-Newton* observations the fitted neutral column is $\approx 2\text{--}3 \times 10^{21} \text{ cm}^{-2}$, which is comparable to the value measured for the least absorbed/peak of the *Chandra* lightcurve. We note that a dominant nonthermal component has been reported in a “recycled” system: the binary radio millisecond pulsar PSR J0024–7204W. The X-ray variability observed in PSR J0024–7204W suggests that the hard X-ray emission is produced by interaction between the pulsar wind and matter from the secondary star, which occurs much closer to the companion star than the millisecond pulsar (Bogdanov et al. 2005). The previously observed hard tail in 4U 2129+47 might have been a similar phenomenon.

What remains ambiguous is whether the associated drop in the 0.5–2 keV absorbed flux is solely related to the vanishing of the hard tail, or whether additional cooling of the neutron star has occurred, or continues to occur. Although the soft X-ray flux has clearly declined from the *Chandra* observations to the *XMM-Newton* observations, there is no evidence for a decline between the 2005 and 2007/2008 observations. The initial drop of the soft X-ray flux is consistent with solely the loss of the hard tail for some parameter regimes of this component; however, for the best-fit parameters, additional cooling would have had to occur.

We note that the expected luminosity of 4U 2129+47 due to neutron star cooling has recently been discussed by Heinke et al. (2009). Even though 4U 2129+47 is among the brighter of the 23 quiescent sources presented by Heinke et al. (2009), the degree to which it is “too faint”, and thus requires “non-standard” cooling (kaon cooling, pion cooling, etc.; see Heinke et al. 2009 and references therein) relies on the rather uncertain average heating history of 4U 2129+47, and the knowledge that the bulk of the observed soft X-ray emission was *not* due to residual accretion. We note that any implied reduction of the soft X-ray emission of 4U 2129+47, or any continued cooling observed in the future, increases the need to invoke “non-standard” cooling mechanisms for this system, and further limits the parameter space for the long term average heating that would allow for “standard” cooling.

A question also arises as to whether or not the loss of the hard X-ray tail is in any way related to the unusual timing residuals associated with the 2005 *XMM-Newton* observations (B07). Strong deviations from a simple linear or quadratic ephemeris have also been noted for the bursting neutron star system EXO 0748–676 (Wolff et al. 2009),

with these changes possibly being correlated with the duration of the eclipse as viewed by the *Rossi X-ray Timing Explorer* (RXTE). (Note that comparable eclipse duration changes, < 20 s, observed in EXO 0748–676 are too small to have been seen in 4U 2129+47 with our observations.) Wolff et al. (2009) hypothesize that these eclipse duration and ephemeris changes are related to magnetic activity within the secondary. We note, however, that over a comparable five year span, the peak-to-peak residuals of EXO 0748–676 (70 s) are three to four times smaller than the peak-to-peak residuals seen in 4U 2129+47 (200–300 s). Furthermore, the trend of ephemeris timing residuals of EXO 0748–676 are more persistently in one direction (although deviations do occur) than those that we show in Fig. 2 (compare to Fig. 4 of Wolff et al. 2009).

In our work, we confirmed the strong deviations of two 2005 XMM-Newton eclipses from any linear or quadratic ephemeris, however, this deviation has only been observed

once since 1982. Rather than presuming ephemeris residuals comparable to those of EXO 0748–676, given the optical observations (e.g. Garcia & Grindlay 1987; Bothwell et al. 2008), we instead have adopted the hypothesis of a triple system. Given the lack of constraints, however, we had to assume a sinusoidal function for simplicity. With this assumption, the chance of detecting a maximal time deviation and a minimal deviation should be equal. The rare presence of the strong deviation may be due to a large eccentricity of the third body orbit, so that the third star rarely interacts strongly with the inner binary system. The third body orbital period was estimated to be around 175 days, but can not be uniquely determined with the current observations. In order to confirm and accurately determine the orbital period of the third body, further observations are required. Such future observations could also address whether the soft X-ray flux of 4U 2129+47 has continued to drop, and whether the hard tail and sinusoidal modulation remain absent.

REFERENCES

- Blandford, R. D., & Begelman, M. C. 1999, MNRAS, 303, L1
 Davis, J. 2001, ApJ, 548, 1010
 Bogdanov, S., Grindlay, J. E., & van den Berg, M. 2005, ApJ, 630, 1029
 Bothwell, M.S., Torres, M.A.P., Garcia, M.R., & Charles, P.A. 2008, A&A, 485, 773
 Bozzo, E., Falanga, M., Papitto, A., et al. 2007, A&A, 476, 301 (B07)
 Campana, S., Stella, L., Mereghetti, S., et al. 1998, ApJ, 499, L65
 Campana, S., & Stella, L. 2000, ApJ, 541, 849
 Chevalier, C., Ilovaisky, S. A., Motch, C., et al. 1989, A&A, 217, 108
 Cottam, J., Sako, M., Kahn, S.M., Paerels, F., & Liedahl, D.A. 2001, ApJ, 557, L101.
 Cowley, A. P., & Schmidtke, P C. 1990, AJ, 99, 678
 Esin, A. A., McClintock, J. E., & Narayan, R. 1997, ApJ, 489, 865
 Forman, W., Jones, C., Cominsky, L., et al. 1978, ApJ, 38, 357
 Garcia, M. R., & Grindlay, J. E. 1987, ApJ, 313, L59
 Garcia, M. R., Bailyn, C.D., Grindlay J. E., & Molnar, L. A. 1989, ApJ, 341, L75
 Heinke, C.O., Rybicki, G.B., Narayan, R., & Grindlay, J.E. 2006, ApJ, 644, 1090
 Heinke, C.O., Jonker, P.G., Wijnands, R., Deloye, C.J., & Taam, R.E. 2009, ApJ, 691, 1035
 Heinz, S., & Nowak, M. A. 2001, MNRAS, 320, 249
 Houck, J.C., & Denicola, L.A. 2000, in ASP Conf. Ser. 216: Astronomical Data Analysis Software and Systems IX, Vol. 9, 591
 Horne, K., Verbunt, F., & Schneider, D. P. 1986, MNRAS, 218, 63
 Kaluzny, J. 1988, Acta Astron., 38, 207
 McClintock, J. E., London, R. A., Bond, H. E., & Grauer, A. D. 1982, ApJ, 258, 245 (MC82)
 Nowak, M. A., Heinz, S., & Begelman, M.C. 2002, ApJ, 573, 778 (N02)
 Nowak, M. A., Wilms, J., Heinz, S., Pooley, G., Pottschmidt, K., & Corbel, S. 2005, ApJ, 626, 1006.
 Parmar, A. N., Oosterbroek, T., Del Sordo, S., et al. 2000, A&A, 356, 175
 Thorstensen, J., Charles, P., Bowyer, S., et al. 1979, ApJ, 233, L57
 White, N.E., & Holt, S.S. 1982, ApJ, 257, 318.
 Wilms, J., Allen, A., & McCray, R. 2000, ApJ, 542, 914.
 Wolff, M.T., Ray, P.S., Wood, K.S., & Hertz, P.L. 2009, ApJ, in press.
 Ulmer, M. P., Shulman, S., Yentis, D., et al. 1980, ApJ, 235, L159
 Zavlin, V.E., Pavlov, G.G., & Shibano, Y.A. 1996, A&A, 315, 141.

TABLE 2
BEST-FIT SPECTRAL PARAMETERS

Parameters	XMM-Newton (2007/2008)			XMM-Newton (2005)			Chandra (Γ free)	
	(no powerlaw) ^a	(no powerlaw) ^b	($\Gamma = 2$, fixed)	(no powerlaw)	(no powerlaw)	(no powerlaw) ^a		(no powerlaw) ^b
N_{H} (10^{22} cm^{-2})	$0.21^{+0.02}_{-0.03}$	0.24 ± 0.03	0.29 ± 0.03	0.32 ± 0.03	$0.26^{+0.07}_{-0.06}$	$0.33^{+0.11}_{-0.06}$	0.37 ± 0.07	$0.39^{+0.18}_{-0.11}$
kT_{bb} (keV)	$0.213^{+0.007}_{-0.006}$	$0.202^{+0.011}_{-0.010}$	$0.210^{+0.015}_{-0.015}$	$0.210^{+0.033}_{-0.043}$
R_{bb} (km) ^c	1.8 ± 0.2	$2.0^{+0.4}_{-0.2}$	$1.9^{+0.6}_{-0.4}$	$2.5^{+2.3}_{-0.9}$
A_{PL} ($10^{-5} \gamma/\text{keV}/\text{cm}^2/\text{sec}$) ^d	...	$0.3^{+0.3}_{-0.2}$	$1.5^{+7.4}_{-1.3}$
Γ	...	2	$2^{+1.5}_{-1.6}$...
$\log T_{eff}$ (log K)	6.37 ± 0.06	6.00 ± 0.03	...	$6.39^{+0.16}_{-0.13}$	5.99 ± 0.06	...
R_{NS}^{∞} (km) ^e	$5.3^{+0.1}_{-0.3}$	$16.7^{+2.8}_{-2.6}$...	$5.2^{+1.5}_{-0.2}$	$18.2^{+7.6}_{-5.8}$...
$\chi^2/\text{d.o.f.}$	62.6/73	57.8/72	56.0/73	55.8/73	32.2/37	33.1/37	32.6/37	10.7/17
$F_{0.5-2 \text{ keV}}^f$ ($10^{-14} \text{ erg cm}^{-2} \text{ s}^{-1}$)	7.7 ± 0.1	7.7 ± 0.1	7.7 ± 0.1	7.7 ± 0.1	7.5 ± 0.3	7.5 ± 0.3	7.5 ± 0.3	12 ± 1
$F_{0.5-10 \text{ keV}}^f$ ($10^{-14} \text{ erg cm}^{-2} \text{ s}^{-1}$)	8.0 ± 0.5	8.6 ± 0.6	8.1 ± 0.5	8.0 ± 0.5	7.8 ± 0.8	7.9 ± 0.8	7.8 ± 0.8	16 ± 2
$F_{0.5-2 \text{ keV}}^g$ ($10^{-13} \text{ erg cm}^{-2} \text{ s}^{-1}$)	$1.29 \pm 0.03(\pm 0.05)$	$1.40 \pm 0.03(\pm 0.08)$	$1.64 \pm 0.03(\pm 0.09)$	$1.78 \pm 0.04(\pm 0.09)$	$1.4 \pm 0.1(\pm 0.2)$	$1.8 \pm 0.1(\pm 0.2)$	$1.9 \pm 0.1(\pm 0.2)$	$2.8 \pm 0.2^{(+1.1)}_{(-0.4)}$
$F_{0.5-10 \text{ keV}}^g$ ($10^{-13} \text{ erg cm}^{-2} \text{ s}^{-1}$)	$1.32 \pm 0.06(\pm 0.05)$	$1.49 \pm 0.06(\pm 0.08)$	$1.68 \pm 0.06(\pm 0.09)$	$1.81 \pm 0.04(\pm 0.09)$	$1.4 \pm 0.1(\pm 0.2)$	$1.8 \pm 0.1(\pm 0.2)$	$2.0 \pm 0.1(\pm 0.2)$	$3.2 \pm 0.2^{(+1.3)}_{(-0.4)}$

NOTE. — Parameter errors are 90% confidence for one interesting parameter (i.e., $\Delta\chi^2 = 2.71$). Flux errors are 68% confidence (values in parantheses are systematic errors - see Appendix).

^a NSA model, assuming a fixed neutron star mass of $1.4 M_{\odot}$

^b NSATMOS model, assuming a fixed neutron star mass of $1.4 M_{\odot}$

^c Neutron star radius assuming a distance of 6.3 kpc

^d Powerlaw normalization at 1 keV.

^e Lower limit constrained to > 5 .

^f Absorbed flux.

^g Unabsorbed flux.

TABLE 3
BEST-FIT NSATMOS SPECTRAL PARAMETERS FOR A JOINT FIT OF THE *Chandra* AND *XMM-Newton* SPECTRA

Parameters	Chandra	XMM-Newton	
		(2005)	(2007/2008)
N_{H} (10^{22} cm^{-2})	0.36 ± 0.01	0.36 ± 0.04	$0.33^{+0.02}_{-0.04}$
$\log T_{eff}$ (log K) ^a	$6.48^{+0.02}_{-0.07}$	$6.45^{+0.02}_{-0.13}$	$6.45^{+0.02}_{-0.20}$
A_{PL} ($10^{-5} \gamma/\text{keV}/\text{cm}^2/\text{sec}$)	$1.2^{+0.3}_{-0.4}$
M_{NS} (M_{\odot})	...	$1.66^{+0.02}_{-0.58}$...
R_{NS} (km)	...	$5.55^{+0.01}_{-0.06}$...
$F_{0.5-10 \text{ keV}}^b$ ($10^{-13} \text{ erg cm}^{-2} \text{ s}^{-1}$)	$3.2 \pm 0.2(\pm 0.3)$	$2.0 \pm 0.1(\pm 0.2)$	$1.9 \pm 0.1(\pm 0.1)$
$\chi^2/\text{d.o.f.}$...	99.6/128	...

NOTE. — A $\Gamma \equiv 2$ powerlaw was included for only the *Chandra* spectra. The neutron star distance was fixed to 6.3 kpc. Parameter errors are 90% confidence for one interesting parameter (i.e., $\Delta\chi^2 = 2.71$). Flux errors are 68% confidence (values in parantheses are systematic errors - see Appendix).

^a Upper bound of the $\log T_{eff}$ is constrained to be < 6.5 .

^b Unabsorbed flux.

APPENDIX
FLUX ERROR BARS

It is impossible to uniquely invert the (imperfectly known) X-ray detector response matrices to yield a completely model-independent, yet accurate, estimate of the detected flux for an observed source. This also leads to difficulties in deriving error bars for any estimate of the flux. Here we use the fact that the “deconvolved flux” is a reasonably close estimate of the “model flux” to estimate the error bars on this latter quantity as presented in Table 2. Specifically, we define the “deconvolved photon flux” in Pulse Height Analysis (PHA) channel h as:

$$F(h) = \frac{C(h) - B(h)}{T \int R(E, h) A(E) dE} , \quad (\text{A1})$$

where $C(h) - B(h)$ are the background subtracted counts in channel h , T is the observation integration time, $R(E, h)$ is the detector response matrix, and $A(E)$ is the detector effective area. (See Davis 2001 for a more in depth discussion of the meanings of these terms.) This is the same deconvolution used to create Fig. 3, and it is independent of assumed model. The deconvolved energy flux in a given band is then determined by multiplying the above photon flux by the midpoint energy of the PHA bin (determined from the EBOUNDS array of the response matrix), and summing over the channels within the given energy band of interest. The error is determined from the sum in quadrature of the error from each non-zero bin, which in turn is determined from the counting statistics of the source and background.

This flux estimate can be compared to the model photon flux, which is determined by integrating the best fit model over the energy band of interest. For all the models considered in this paper, these two estimates agree to within 3% when applied to the *absorbed* 0.5–2 keV flux and agree to within 9% when applied to the *absorbed* 0.5–10 keV flux. We therefore use the model flux as our flux estimate; however, we use the deconvolved flux error bars, scaled by the ratio of model to deconvolved flux, as the estimate of our flux errors. Note that with this definition it is possible for the 0.5–10 keV flux to have a -1σ bound below that of the 0.5–2 keV flux. This might be indicative of unmodeled flux in the 3–10 keV band; however, we lack the statistics to describe the flux in this band with any degree of accuracy. From this point of view, the flux estimate with the least amount of systematic uncertainty is the 0.5–2 keV absorbed flux.

When determining the statistical errors on the unabsorbed flux, we further scale the above error estimates by the energy-dependent ratio of the unabsorbed to absorbed model flux. The systematic error bars on the unabsorbed fluxes are then determined individually for each spectral model. We freeze the fitted value of the neutral column at its $\pm 1\sigma$ limits, refit the spectra, and then determine the fluxes as described above. The deviations of the unabsorbed fluxes at these two absorption limits compared to the flux obtained when using the best fit parameter values are assigned as the systematic error bars. Note that such systematic errors are for a given model, and do not reflect the systematic errors on the unabsorbed fluxes obtained from comparing different assumed spectral models.

For the cases of fitting the spectra with a blackbody and a powerlaw we employ one other estimate of the flux error bars for the individual model components. ISIS allows one to set any given parameter to be an arbitrary function of any other set of fit parameters. It therefore was straightforward to recast the spectral fit from dependence upon blackbody normalization and temperature to dependence upon unabsorbed 0.5–10 keV blackbody flux and temperature (i.e., the blackbody normalization can be written as a function of those two parameters). Likewise, the powerlaw fit parameters were recast to depend upon unabsorbed 0.5–10 keV flux and powerlaw slope. We thus were able to use direct fitting methods to generate the error contours shown in Fig. 4.

APPENDIX
FLUX ERROR BARS

It is impossible to uniquely invert the (imperfectly known) X-ray detector response matrices to yield a completely model-independent, yet accurate, estimate of the detected flux for an observed source. This also leads to difficulties in deriving error bars for any estimate of the flux. Here we use the fact that the “deconvolved flux” is a reasonably close estimate of the “model flux” to estimate the error bars on this latter quantity as presented in Table 2. Specifically, we define the “deconvolved photon flux” in Pulse Height Analysis (PHA) channel h as:

$$F(h) = \frac{C(h) - B(h)}{T \int R(E, h) A(E) dE} , \quad (\text{A1})$$

where $C(h) - B(h)$ are the background subtracted counts in channel h , T is the observation integration time, $R(E, h)$ is the detector response matrix, and $A(E)$ is the detector effective area. (See Davis 2001 for a more in depth discussion of the meanings of these terms.) This is the same deconvolution used to create Fig. 3, and it is independent of assumed model. The deconvolved energy flux in a given band is then determined by multiplying the above photon flux by the midpoint energy of the PHA bin (determined from the EBOUNDS array of the response matrix), and summing over the channels within the given energy band of interest. The error is determined from the sum in quadrature of the error from each non-zero bin, which in turn is determined from the counting statistics of the source and background.

This flux estimate can be compared to the model photon flux, which is determined by integrating the best fit model over the energy band of interest. For all the models considered in this paper, these two estimates agree to within 3% when applied to the *absorbed* 0.5–2 keV flux and agree to within 9% when applied to the *absorbed* 0.5–10 keV flux. We therefore use the model flux as our flux estimate; however, we use the deconvolved flux error bars, scaled by the ratio of model to deconvolved flux, as the

estimate of our flux errors. Note that with this definition it is possible for the 0.5–10 keV flux to have a -1σ bound below that of the 0.5–2 keV flux. This might be indicative of unmodeled flux in the 3–10 keV band; however, we lack the statistics to describe the flux in this band with any degree of accuracy. From this point of view, the flux estimate with the least amount of systematic uncertainty is the 0.5–2 keV absorbed flux.

When determining the statistical errors on the unabsorbed flux, we further scale the above error estimates by the energy-dependent ratio of the unabsorbed to absorbed model flux. The systematic error bars on the unabsorbed fluxes are then determined individually for each spectral model. We freeze the fitted value of the neutral column at its $\pm 1\sigma$ limits, refit the spectra, and then determine the fluxes as described above. The deviations of the unabsorbed fluxes at these two absorption limits compared to the flux obtained when using the best fit parameter values are assigned as the systematic error bars. Note that such systematic errors are for a given model, and do not reflect the systematic errors on the unabsorbed fluxes obtained from comparing different assumed spectral models.

For the cases of fitting the spectra with a blackbody and a powerlaw we employ one other estimate of the flux error bars for the individual model components. ISIS allows one to set any given parameter to be an arbitrary function of any other set of fit parameters. It therefore was straightforward to recast the spectral fit from dependence upon blackbody normalization and temperature to dependence upon unabsorbed 0.5–10 keV blackbody flux and temperature (i.e., the blackbody normalization can be written as a function of those two parameters). Likewise, the powerlaw fit parameters were recast to depend upon unabsorbed 0.5–10 keV flux and powerlaw slope. We thus were able to use direct fitting methods to generate the error contours shown in Fig. 4.